Improving the Calibration of Impact Plate Bedload Monitoring Systems by Filtering Out Acoustic Signals from Extraneous Particle Impacts

Tobias Nicollier[1,2], Gilles Antoniazza[1,3], Dieter Rickenmann[1], Arnd Hartlieb[3], James W. Kirchner[1,2,5]

[1] Swiss Federal Research Institute WSL, Birmensdorf, Switzerland

[2] Dept. of Environmental System Sciences, ETH Zürich, Zürich, Switzerland

[3] Institute of Earth Surface Dynamics (IDYST), University of Lausanne, Lausanne, Switzerland

[4] Laboratory of Hydraulic and Water Resources Engineering, Technical University of Munich, Obernach, Germany

[5] Dept. of Earth and Planetary Science, University of California, Berkeley, California, USA

Correspondence to: Tobias Nicollier, Swiss Federal Research Institute (WSL), Mountain Hydrology and Mass Movements, 8903 Birmensdorf, Switzerland. E-mail: tobias.nicollier@wsl.ch. Phone: +41 77 437 35 77

Keywords: Bedload transport; Swiss plate geophone; Flume experiments; Noise filtering; Global calibration relationship

Key Points

1. Seismic waves generated by impacting bedload particles can propagate over several plates of the Swiss plate geophone system
2. Flume experiments enabled to characterize the signal originating from impacts either on neighboring plates or on the neighboring flume bed
3. A filter method eliminating apparent impacts was developed and applied to field calibration datasets, improving site-to-site comparisons

Abstract

The spatio-temporal variability of bedload transport processes poses considerable challenges for bedload monitoring systems. One such system, the Swiss plate geophone (SPG), has been calibrated in several gravel-bed streams using direct sampling techniques. The linear calibration coefficients linking the signal recorded by the SPG system to the transported bedload can vary between different monitoring stations by about a factor of six, for reasons

that remain unclear. Recent controlled flume experiments allowed us to identify the grain-size distribution of the transported bedload as a further site-specific factor influencing the signal response of the SPG system, along with the flow velocity and the bed roughness. Additionally, impact tests performed at various field sites suggested that seismic waves generated by impacting particles can propagate over several plates of an SPG array, and thus potentially bias the bedload estimates. To gain an understanding of this phenomenon, we adapted a test flume by installing a partition wall to shield individual sensor plates from impacting particles. We show that the SPG system is sensitive to seismic waves that propagate from particle impacts on neighboring plates or on the concrete bed close to the sensors. Based on this knowledge, we designed a filter method that uses time-frequency information to identify and eliminate these "apparent" impacts. Finally, we apply the filter to four field calibration datasets and show that it significantly reduces site-to-site differences between calibration coefficients and enables the derivation of a single calibration curve for total bedload at all four sites.

Plain Language Summary

Flood-related hazards like bedload transport can potentially constitute a significant threat to human life and infrastructure. The spatio-temporal variability of these processes poses considerable challenges for bedload monitoring systems such as the Swiss plate geophone (SPG). Calibration relationships linking the signal recorded by the SPG system to the transported bedload can vary significantly between different monitoring stations, possibly due to site-specific factors such as the coarseness of the bedload, the flow velocity and the bed roughness. Additionally, impact tests performed at various field sites suggested that seismic waves generated by impacting particles can be detected simultaneously by multiple sensors, and thus potentially bias the bedload estimates. To gain an understanding of this phenomenon, we adapted a test flume by installing a partition wall to shield individual sensor plates from impacting particles. We show that the SPG system is sensitive to seismic waves generated by impacts either on neighboring plates or on the flume bed close to the sensors. Based on this knowledge, we designed a filter method that uses time-frequency information to identify and eliminate these "apparent" impacts. Finally, we apply the filter to four field calibration datasets and show that filtering significantly reduces site-to-site differences between calibration relationships.

1 Introduction

Various climate-related indicators suggest that European Alpine water courses will be substantially altered by climate change (FOEN, 2021; Stoffel et al., 2014). In recent times, more frequent flooding has been observed in several parts of Europe, affecting society as well as ecosystems (Badoux et al., 2014; Blöschl et al., 2020). In addition to surface runoff, sediment availability also is expected to increase, especially in glacierized catchments (FOEN, 2021). Due to increased erosion in winter, melting glaciers, or more recurrent landslides, larger amounts of sediment will be delivered to channels and potentially mobilized during future, stronger precipitation events (Benateau et al., 2019; Hirschberg et al., 2020; Speerli et al., 2020). Flood-related hazards like bedload transport pose a significant threat to human life and infrastructure, especially in small alpine catchments (Badoux et al., 2014). However, monitoring and predicting such bedload transport processes still represents a considerable challenge because of their large spatio-temporal variability (e.g. Mühlhofer, 1933; Einstein, 1937; Reid et al., 1985; Habersack et al., 2008; Rickenmann, 2018; Ancey; 2020).

Traditional direct bedload sampling methods such as retention basins, slot samplers or mobile bag samplers (e.g. Helley and Smith, 1971) have a limited resolution in space and time, determined by factors such as the sampler capacity (e.g. Habersack et al., 2017), the flow conditions (e.g. Bunte et al., 2004) or the bed material texture (Camenen et al., 2012). In the last decade or so, more effort was put into the development of indirect bedload surrogate monitoring technologies, in order to overcome some of the limitations of direct methods (Gray et al., 2010; Rickenmann, 2017). This is achieved by using active sensors, such as acoustic Doppler current profilers (aDcp; Le Guern et al., 2021), that emit acoustic signals, or by using passive sensors that record acoustic or elastic waves generated by bedload. Seismometers installed on streambanks (Roth et al., 2016, Dietze et al., 2019; Gimbert et al., 2019) and underwater microphones (Thorne, 1986; Geay et al., 2017) both record the self-generated noise produced by the interparticle collisions of moving bedload material. Devices such as the Japanese pipe microphone (Mizuyama et al., 2010a, b; Mao et al., 2016) or the impact plate system equipped with either a microphone, a piezoelectric sensor, or a geophone (e.g. Rickenmann and McArdell, 2007; Krein et al., 2008; Raven et al., 2010; Hilldale et al., 2015; Wyss et al., 2016a; Kuhnle et al., 2017; Koshiba et al., 2018), record the vibration or sound produced by the elastic impact of particles on a metallic structure.

Surrogate monitoring techniques such as these offer many advantages over the traditional direct methods in terms of robustness, spatial coverage and temporal resolution. However, numerous recent studies have demonstrated that direct methods are still indispensable to efficiently calibrate impact plates (Rickenmann et al., 2012, 2014; Habersack et al., 2017; Kreisler et al., 2017; Nicollier et al., 2021; Antoniazza et al., in review), hydrophones (Geay et al., 2017) and pipe microphones (Mizuyama et al., 2010a; Dell'Agnese et al., 2014; Mao et al., 2016). Typically, linear or power-law calibration relationships are developed between measured signal properties and bedload transport characteristics. Such calibration equations enable spatio-temporal estimates of bedload fluxes and the detection of the start and end of bedload transport. However, each site must be individually calibrated, because the current bedload surrogate measuring techniques lack generally applicable signal-to-bedload-flux calibration equations that are valid across multiple field sites.

Surrogate monitoring techniques can also be impaired by ambient noise sources. Water turbulence, for example, can significantly reduce the performance of aDcp systems (Conevski et al. 2018), seismometers (Roth et al., 2016) or hydrophones (Gray et al., 2010; Geay et al., 2017). In addition, anthropogenic sources (Barrière et al., 2015) and rainfall (Roth et al., 2016) can both contaminate the recorded signal. Recent studies report the successful implementation of time-frequency based methods to increase the signal-to-noise ratio and improve the detectability of bedload particles using pipe hydrophones (Choi et al., 2020) and impact plate systems (Barrière et al. 2015; Koshiba & Sumi, 2018).

Among the passive monitoring techniques, the Swiss plate geophone (SPG) system has been deployed and tested in 21 steep gravel-bed streams and rivers, mostly in the European Alps (Rickenmann, 2017). Although the similarities between calibration measurements from various field sites are encouraging, it is not well understood why the linear calibration coefficients can vary by about a factor of 20 among individual samples from different sites, or by about a factor of six among the mean values from different sites, excluding the special case of the ephemeral Nahal Eshtemoa stream (Rickenmann et al., 2014; Rickenmann & Fritschi, 2017). Wyss et al. (2016b) found that the flow velocity can matter, with higher flow velocities inducing a weaker signal response. Another important site-dependent factor influencing the signal response is the grain-size distribution (GSD) of the transported bedload (Nicollier et al., 2021): coarser grain mixtures yield stronger signal responses, per unit bedload weight, in the SPG system. SPG systems have typically been assumed to be insensitive to background noise

such as water turbulence, because of damping by the elastomer supports for the impact plates, and due to the high threshold value used for impulse counts (Wyss et al., 2016b). However, recent impact tests performed at various field sites suggest that the energy released by an impact on a plate can propagate over several plate lengths and contaminate the signals from multiple sensors (Antoniazza et al., 2020).

Here we examine the propagation of seismic waves released by impacts as a possible noise source affecting the signal response of the SPG system and biasing calibration relationships. We characterize the propagated waves detected by the SPG system using field and flume calibration data, in order to distinguish signal packets originating from measurement artifacts versus real bedload transport. Furthermore, we analyze a set of full-scale controlled flume experiments conducted at the Obernach flume facility, where we used a partition wall to shield one sensor plate from impacting bedload particles. Finally we propose a signal processing method that aims to isolate each sensor plate from propagating waves and apply it to field calibration data. Hence, the objectives of this study are (i) to detect and characterize parts of the raw signal (or packets) recorded by the SPG system that originated as impacts occurring beyond each individual plate, (ii) to quantify the number of (unwanted) "apparent" packets generated by waves propagated from these impacts, as function of the size of the transported bedload material, (iii) to develop a filter method that distinguishes real from apparent packets and (iv) to show that filtering calibration data from four field sites reduces the differences between the site-specific calibration coefficients, and enables the derivation of a generic calibration equation (or signal conversion procedure) valid for all four sites.

2 Methods

2.1 The SPG System

The Swiss plate geophone (SPG) system is based on a geophone sensor fixed under a steel plate of standard dimensions 492 mm x 358 mm x 15 mm (Rickenmann, 2017). The geophone (GS-20DX by Geospace technologies; www.geospace.com) uses a magnet moving inside an inertial coil (fixed on springs) as an inductive element. The voltage induced by the moving magnet is directly proportional to the vertical velocity resulting from particle impacts on the plate. Typically, a SPG array includes several plates next to each other, acoustically isolated by elastomer elements. The array is either embedded in a concrete sill or fixed at the downstream wall of a check dam. A detailed description of the SPG system can be found in Rickenmann et al. (2014).

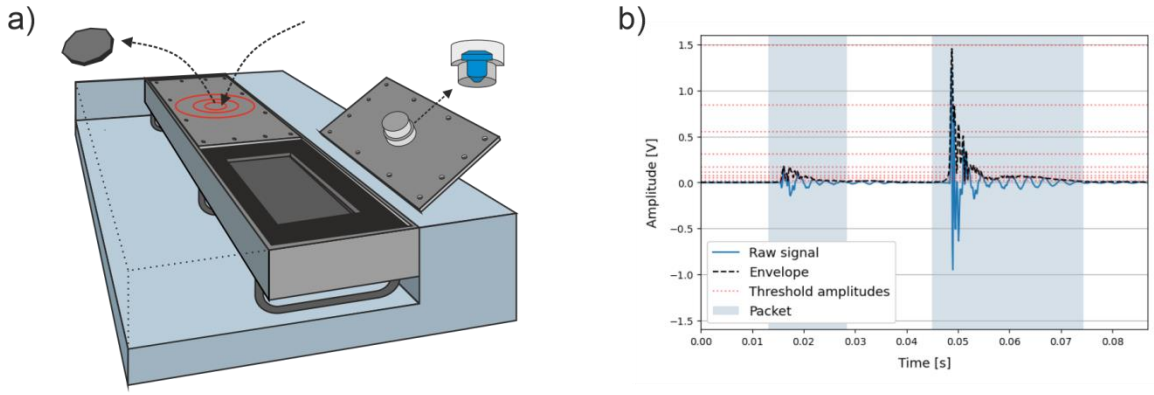

Figure 1. (**a**) SPG array embedded in concrete including two steel plates, each equipped with a uniaxial geophone sensor fixed in a watertight aluminum box attached to the underside of the plate. The plates are acoustically isolated from each other by elastomer elements (black). (**b**) Example of two packets (light blue area) detected by the SPG system. The start of a packet begins 20 time steps before the signal envelope crosses the lowest amplitude threshold of 0.0216 V and ends 20 time steps after the last crossing of the lowest amplitude threshold of 0.0216 V.

Due to data storage limitations, field stations usually do not continuously record the full raw 10 kHz geophone signal. Instead, it is typically pre-processed, and summary values, such as the maximum amplitude and the number of impulses, are recorded at one-minute intervals. However, for the relatively short duration of a single calibration measurement, ranging from a few seconds to one hour, the full raw signal is stored and processed later. Wyss et al. (2016a) introduced the packet-based amplitude histogram method to derive grain-size information from the geophone signal. Wyss et al. (2016a) define a packet (see Figure 1) as a brief interval, typically lasting 5 to 10 milliseconds, reflecting a single impact of a particle on a plate; it begins and ends when the signal envelope crosses a threshold amplitude of 0.0216 V. The signal envelope is computed with the Hilbert transform (Jones et al., 2002), which compensates for the asymmetric offset of the raw seismic signal around the zero-amplitude level. Each packet's maximum amplitude is then used to assign it to a predefined amplitude class (AC; Table 1), yielding a packet-based amplitude histogram (e.g., Figure 4 of Wyss et al., 2016a). As in the study by Wyss et al. (2016a), each amplitude class j is related to a corresponding grain-size class through the following relationship between the mean amplitude $A_{m,j}$ [V] and the mean particle size $D_{m,j}$ [mm].

$$A_{m,j} = 4.6 \cdot 10^{-4} \cdot {D_{m,j}}^{1.71} \quad (1)$$

196 The grain-size classes are delimited by the size of the meshes used to sieve the bedload
197 samples obtained during field calibration measurements. In the present study, we have
198 extended the seven classes used by Wyss et al. (2016a) to ten classes, to examine in more
199 detail the behavior of larger bedload particles and their effect on the signal response. Wyss et
200 al. (2016a) showed that the packet-based amplitude histogram method provides reasonable
201 estimates of the fractional bed load mass for the Erlenbach calibration measurements. Since
202 2016, in addition to the summary values, sections of the raw signal corresponding to packets,
203 as well as their time of occurrence, are being stored at multiple field monitoring stations. To
204 facilitate its implementation at the field stations and to limit the required computing power,
205 the filtering method described in this study is based on packet information only.
206
207 **Table 1.** *Characteristics of the Amplitude Classes (AC) j*

AC (j) [-]	Lower threshold [V]	$A_{m,j}$ [V]	Lower sieve size [mm]	$D_{m,j}$ [mm]
1	0.0216	0.0336	9.5	12.30
2	0.0527	0.0608	16.0	17.40
3	0.0707	0.0894	19.0	21.80
4	0.1130	0.1381	25.0	28.10
5	0.1670	0.2272	31.4	37.60
6	0.3088	0.4112	45.0	53.20
7	0.5489	0.6783	63.0	71.29
8	0.8378	1.1189	80.7	95.49
9	1.4919	1.8453	113.0	127.87
10	2.2760	(3.0442)	144.7	(171.53)

208 *Note.* Amplitude classes (AC) *j* derived from sieve mesh sizes (for classes 1 to 7) and from Equation (1)
209 according to Wyss et al. (2016a), including mean amplitude $A_{m,j}$ and mean particle diameter $D_{m,j}$. Particles in
210 classes 8 to 10 were manually sorted on the basis of linearly extrapolated $D_{m,j}$ values. The values of $A_{m,j}$ *and* $D_{m,j}$
211 for the largest class (10) in brackets are estimates.
212
213 Calibration coefficients linking the recorded packet rate *PACKT* to the measured total bedload
214 flux q_b can be obtained from the following power-law regression equation,
215
216 $$PACKT = a \cdot {q_b}^b \quad , \tag{2}$$
217
218 where a is the linear coefficient and b the exponent determined by regression. In Equation (2),
219 q_b is expressed in kg m^{-1} s^{-1} and *PACKT* is expressed in packets m^{-1} s^{-1}. Because each plate is
220 0.5 m wide, PACKT equals twice the packet generation rate for an individual plate, and q_b is
221 twice the transport rate (in kg s^{-1}) measured across the width of each plate. To facilitate
222 comparisons among calibration coefficients a from different field sites, we also consider the
223 linear form (b = 1) of Equation (2), which yields calibration coefficients a that are comparable

to the linear calibration coefficient k_b with units [kg^{-1}] determined in previous studies employing the SPG system (e.g. Rickenmann et al., 2014; Wyss et al., 2016b).

To determine the coefficient *a* and exponent *b* of Equation (2), we used the *reduced major axis* (*RMA*) instead of the ordinary least squares (OLS) fit. The RMA regression has the advantage of defining a bivariate relationship with a unique line (Harper, 2014). Our choice of this method assumes that errors contaminate both the sampled bedload (e.g. due to an incorrect positioning of the sampler) and the recorded signal, which is influenced by the impact location on a given impact plate, the type of particle motion, and the impact velocity (Rickenmann & McArdell, 2008), all factors that cannot be quantified, particularly under field conditions. Since we use log-log rating plots, we also improved the estimates by applying a bias correction factor, as suggested by Ferguson (1986).

We use a further calibration coefficient in order to illustrate the increasing importance of energy propagation with increasing particle diameter during flume experiments. The coefficient α_{tot}, as defined by Wyss et al. (2016c), describes the detectability of particles for a given class and links the sum of the recorded packets $PACK_j$ over all classes *j* to the total number of particles N_{tot} fed into the flume as follows:

$$\alpha_{\mathrm{tot}} = \frac{\sum_{j=1}^{10} PACK_j}{N_{\mathrm{tot}}} \quad (3)$$

2.2 Seismic Wave Attenuation

Seismic wave attenuation is often quantified using the quality factor, *Q*. The quality factor is dimensionless but material-dependent; it is inversely proportional to the fractional loss of energy per oscillation cycle. Ammon et al. (2020) describe the quality factor as “the ratio of the mass- and spring-related terms to the coefficient of friction, *γ*. *Q* has an inverse relationship with attenuation, such that the smaller *Q* is, the larger is the attenuation. Higher *Q* indicates that friction has less influence on the mass' motion”. More generally, *Q* increases together with the density of the material and the seismic wave speed in the material. Ammon et al. (2020) describe the attenuation of a propagating seismic wave as function of the distance travelled *A(r)* using

$$A(r) = A_0 \, exp\left(\frac{-f\pi r}{cQ}\right), \quad (4)$$

where A_0 is the initial amplitude, f is the frequency, r is the distance travelled by the wave and c is the wave velocity. The filter method described further in this study is based on three qualitative observations. (i) The longer the travel distance of a seismic wave, the stronger is its attenuation. (ii) High frequencies are more effectively attenuated than low frequencies. (iii) In the context of a bedload monitoring station, the elastomer used to acoustically isolate the plates from each other attenuates the signal more strongly than does the steel in the supporting structure and the impact plates.

2.3 Packet Classification

The filtering method presented in this study classifies each packet detected by a geophone sensor into the categories "real" and "apparent". While a "real" packet results from a particle impacting on the plate above a given geophone, an "apparent" packet results from an impact either on a neighboring plate or on the surrounding concrete sill (Figure 2). From Equation (4), one can expect that the travel distance of the seismic wave generated by an impact will be reflected in both the amplitude and the power spectral density of the signal recorded by the SPG. Accordingly, the filtering method is based on the packet information listed in the following subsections. We used the stochastic basin-hopping minimization algorithm described by Wales & Doye (1997) and available on SciPy (https://docs.scipy.org) to find the optimal filter parameters for each individual monitoring station as well as for all stations combined. The coefficient of determination R^2 of Equation 2 was used as the objective function for determining the optimal filter parameters.

2.3.1 Maximum Amplitude of the Envelope

Antoniazza et al. (2020) performed impact experiments at the Albula, the Navisence and the Avançon de Nant field sites in order to quantify the attenuation of the seismic wave propagating along a SPG array. The median attenuation of the seismic wave propagating between the impacted plate and the first neighboring plate (r = 50 cm) was found to range from 83 to 90 %. The maximum amplitude of a given packet $MaxAmp_{\mathrm{env}}$ is compared here to the maximum amplitude recorded by the two closest neighboring geophones $MaxAmp_{\mathrm{env,neighbor}}$ within a predefined time window (see subsection 2.3.4). If larger amplitudes were recorded by neighboring plates, one can expect that the packet was triggered by a propagating wave originating from outside the considered plate. The amplitude information is retrieved from the upper envelope, initially used to delimit the beginning and

end of each packet (Wyss et al., 2016a). Compared to the raw signal, the envelope has the advantage of returning the magnitude of the analytical signal and thus better outlines the waveform by omitting the harmonic structure of the signal.

2.3.2 Centroid Frequency

According to the Hertz contact theory, the frequency at which the geophone plate vibrates will depend on the size of the colliding particle (Johnson, 1985; Thorne, 1986; Bogen & Møen, 2003; Barrière et al., 2015; Rickenmann, 2017). In previous studies, the frequency spectrum of a packet was characterized by the spectral centroid f_{centroid} (Wyss et al., 2016b). It indicates the center of mass of the spectrum and is computed as

$$f_{\text{centroid}} = \frac{\sum f_{\text{n}} \cdot A_{\text{FFT,n}}}{\sum A_{\text{FFT,n}}} \tag{5}$$

where $A_{\text{FFT,n}}$ [V·s] is the Fourier amplitude (computed with the Fast Fourier Transform) corresponding to the frequency f_{n} [Hz]. Before applying the FFT, each packet is preprocessed in two steps. First, the packet is zero-padded on either side to reach the required number sample points. Second, a cosine taper is applied at the edges of the packet, smoothing the transition between the packet and the concatenated zeros. This suppresses spectral leakage and enables the computation of a more accurate frequency spectrum. The single-sided Fourier transform of the processed packet is then computed in order to extract the A_{FFT} and derive the f_{centroid} (Equation 5). For a given Q, high frequencies will be more rapidly attenuated than low frequencies along the travel path of a seismic wave (Equation 4). Here we take advantage of this phenomenon and use f_{centroid} as threshold to define whether a packet- triggering impact took place on a given plate.

2.3.3 Peak Frequency

A further characteristic of the packet's power spectrum used to classify packets is the peak frequency f_{peak}. f_{peak} is known as the frequency with the largest amplitude $A_{\text{FFT,n}}$ of the single-sided Fourier transform. Real packets are characterized by high f_{peak} values (> 1500 Hz) for a large range of grain-sizes. This enables a straightforward classification of packets based on a unique threshold. f_{peak} is implemented in the filtering method as secondary step aiming to classify overlapping packets, i.e. packets having an amplitude smaller than the amplitude of the signal recorded by neighboring sensors.

2.3.4 Time Window

Both the comparison of the amplitude with the neighboring signal channels traces and the spectral analysis are carried out within a time window of max. 8 ms around the maximum amplitude of each packet. This section corresponds to the first arrival waveform. In case the packet duration is shorter than 8 ms, the window is reduced to the length of the packet. The aim of this window is twofold. First, it usually avoids overlapping two packets generated close enough in time but on two different plates. Second, in the words of Barrière et al. (2015), "when a sediment particle impacts on the plate, the amplitude and frequency of the first arrival waveform are the two fundamental properties related to the force that the bedload imposes on the plate and the contact time defined as the duration over which the applied impact force is non-zero". Focusing on the first arrival waveform results in a more accurate evaluation of the high-frequency content of the packet.

Note that in previous studies, the traces recorded by the geophones of an SPG array have always been analyzed individually. The novel strategy presented in this study analyzes multiple geophone traces simultaneously, similar to traditional reflection or refraction seismic surveys.

2.3.5 Continuous Wavelet Transform

We attempted to develop a filter method based on the continuous wavelet transform (CWT) as a summary of the time-frequency information of each packet. The CWT was introduced in the field of seismic processing by Goupillaudet al. (1984) and was applied to bedload measurements by Barrière et al. (2015). The advantage of the CWT over the more common FFT is its flexible time–frequency resolution. The CWT is computed with the integral over time of the signal multiplied by scaled and shifted versions of a function called the mother wavelet (Kristeková et al., 2006). The CWT was implemented in the filtering method using the tf_misfit package available on Obspy. As suggested by Barrière et al. (2015), we used the complex Morlet wavelet as the mother wavelet. However, the CWT is computationally more demanding than the FFT and requires too much buffer memory to be applied in real time at monitoring stations when transport rates are high. Additionally the FFT proved to be accurate enough to retrieve the necessary information from the power spectral density of the signal. Nonetheless we continue to use the CWT as a powerful tool to visualize and better understand the time-frequency evolution (i.e., the spectrogram) of each packet.

2.4 Controlled Flume Experiments

The idea for the filter design comes from controlled experiments conducted at the outdoor flume facility of the Oskar von Miller institute of TU Munich in Obernach, Germany. At this facility, we reconstructed the bed characteristics of the Albula, Navisence and Avançon de Nant field sites, one after another, in a test reach with dimensions of 24 m x 1 m equipped with two impact plates (Figure 2). Each site reconstruction used bedload material collected during field calibration measurements, and we adjusted the flow velocity, flow depth, bed roughness to match those field observations. A detailed description of the original flume set-up and the performed experiments can be found in Nicollier et al. (2020). In the present study, we took advantage of the flume to (i) characterize the effect of wave propagation as function of the grain size and (ii) test the filter method. In a first stage, the original set-up was modified and a partition wall was installed in the center of the flume, guiding all of the transported bedload particles over a single plate (plate G2; Figure 2b). The non-impacted plate, G1, served as a reference to characterize apparent packets. Single-grain-size experiments were run with a fixed number of grains for each of the ten particle-size classes, resulting in a total of 51 runs in the modified setup (Tables 1 and 3). The flow velocity was set to 3 m/s to facilitate the transport through the narrower flume section and the bed slope was 4 %. In a second stage, after having defined an optimal filter, we applied it to the entire dataset collected during a series of single-grain-size experiments performed in the original flume set-up between 2018 and 2020 (1095 runs in total, all without the partition wall). Videos recorded at 120 fps during these experiments were used as a supplementary source of information to identify the location of multiple impacts and to classify the generated packets (Figure 2a).

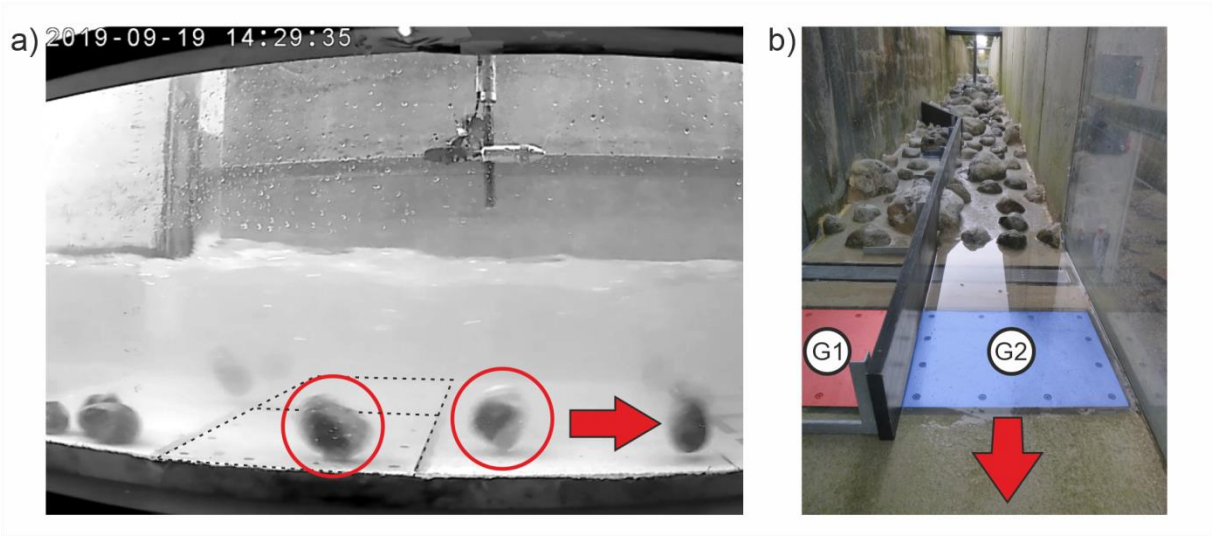

Figure 2 (**a**) Snapshot of a video recording of a single-grain-size experiment using particles of class j=8 in the original flume setup. The dashed black line marks the contour of the two

impact plates. The left circled particle illustrates an impact on a plate, which can lead to the recording of one real packet by G1 and one apparent packet by G2. The right circled particle illustrates an impact on the concrete bed, which can lead to the recording of an apparent packet by both sensors. The magnetic-inductive flow meter used to measure and adjust the flow velocity is visible above the water level. (**b**) Upstream view of the test reach with dimensions of 24 m x 1 m. Grains were fed into the channel 8 m upstream from the SPG system location. The 4 m–long wooden partition wall and the impact plates are decoupled from each other by a 2 mm gap. The sensor plate G1 is shielded from direct particle impacts. However, both plates can detect impacts on the concrete bed. The red arrows indicate the flow direction.

2.5 Field Calibration

After having defined the general structure of the filter, the optimal filter parameters were obtained using calibration data collected at four Swiss bedload monitoring stations equipped with the SPG system (Table 2). The Albula, the Navisence and the Avançon de Nant stations were all calibrated and subsequently replicated in the flume within the frame of the same project. The extensive field calibration dataset from the Erlenbach site was also included to this analysis, in order to test the filter method under different channel and flow characteristics. A calibration consists of the following steps: (i) direct sampling downstream of an impact plate using one of the listed techniques, (ii) synchronous recording of the raw geophone signal, (iii) sieving and weighing the sample according to the ten sieve classes presented in Table 1, (iv) comparing both the fractional and the total bedload mass of each sample to the packet-based amplitude histogram data to derive the corresponding calibration coefficient *a* (Equation 2). A more detailed description of the procedure is reported in Supplementary Information S1. This study focuses on the calibrations for the total bedload mass; the calibrations for individual size classes will be the focus of an upcoming paper.

Table 2. *Channel and Flow characteristics from In Situ Measurements Made During the Calibration Campaigns at the Four Field Sites*

Field site	Location (canton)	Bed slope [%] [a]	Flow velocity V_w [m/s] [b]	No. plates	Year	Technique	No. of samples
Albula [c]	Tiefencastel (Grisons)	0.7	2.6	30	2018	crane-mounted net sampler	51

Navisence [c]	Zinal (Valais)	3	3.2	12	2019	crane-mounted net sampler	80
Avançon de Nant [d]	Plans-sur-Bex (Vaud)	4	1.3	10	2019/2020	manual basket sampler	55
Erlenbach [e]	Alpthal (Schwyz)	16	5	2	Since 2009	automatic basket sampler	123

Note. The year of the field calibration campaigns, the sampling technique and the number of collected samples are indicated.

[a] Gradient measured upstream of the site

[b] Depth-averaged mean flow velocities measured during the calibration measurements

[c] More information available in Nicollier et al. (2021)

[d] More information available in Antoniazza et al. (2021)

[e] More information available in e.g. Rickenmann et al. (2012), Wyss et al. (2016c), Rickenmann et al. (2018)

3 Results

3.1 Identification of Wave Propagation in Flume and Field Data

By synchronizing the videos and the seismic traces recorded during the flume experiments performed without the partition wall, we are able to make a first step towards packet classification. The following observations can be made from the example shown in Figure 3. First, in the first 0.06 seconds, Figure 3 shows three impacts on the concrete in the vicinity of the SPG array, detected by both sensors as packets with similarly low amplitudes, and f_{peak} and $f_{centroid}$ values below 900 Hz. Second, between 0.08 and 0.11 seconds, and again between 0.17 and 0.19 seconds, Figure 3 shows impacts on a G2 and G1, respectively, detected by the corresponding sensor as real packets with f_{peak} and $f_{centroid}$ ranging from 1300 to 2000 Hz. Third, these same impacts are detected by the neighboring sensor as apparent packets with f_{peak} and $f_{centroid}$ values ranging from 250 to 1000 Hz. The attenuation of the high frequencies is visible in the spectrograms of these packets, obtained using the continuous wavelet transform. Finally, (iv) the maximum amplitude of the real packets is about three times larger than the maximum amplitude of the corresponding apparent packets.

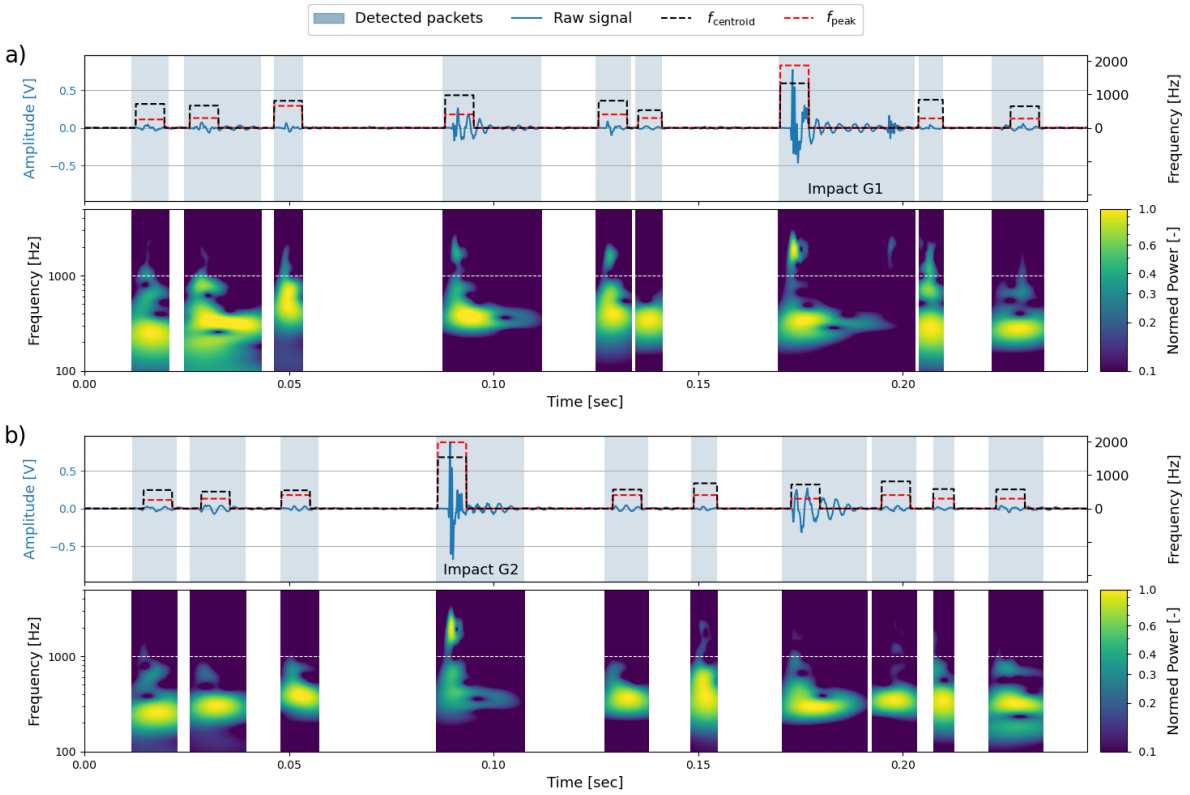

Figure 3. Raw signal recorded by the impact plates (**a**) G1 and (**b**) G2 during single-grain-size flume experiments with particles of class j = 6. Note the maximum 8 ms-long time window around the maximum amplitude of each packet, marked by the dashed red and black lines. The two impacts that occurred on a plate are annotated. Below each seismic trace, the spectrogram derived using the continuous wavelet transform is shown for each packet. Each spectrogram section is normed with the highest power detected for the corresponding packet, in order to improve the readability of the low-amplitude packets.

The flume is equipped with only two impact plates, whereas field stations can include up to 72 plates (Hilldale et al., 2015). The examples from the Navisence site (Figure 4) illustrate the increasing significance of the seismic wave propagation with the number of plates. Note that the exact impact location cannot be verified in the field. Therefore, the examples in Figure 4 only serve as illustrations of the occurrence of wave propagation, and do not constrain the filter design. In Figure 4b, the impact on plate G7 generated an excursion of the signal of about 3.2 V (equivalent to a particle with 17.7 cm diameter) and was detected by 11 out of 12 plates along the 6 m-long transect. In Figure 4c, all 12 plates have detected the same propagating seismic wave. The parabolic shift of the arrival time and the regular shape of the signal suggest that the impact took place on the concrete in the vicinity of G3. These two field

examples are also consistent with the packet characteristics described in Figure 3: impacts on a plate generate centroid and peak frequencies exceeding ~1000 Hz and maximum amplitudes that are much greater than those on adjacent plates, whereas impacts on the concrete generate lower peak frequencies, and a more uniform distribution of maximum amplitudes across the plates. Finally, note that all the packets originating from a same impact do overlap.

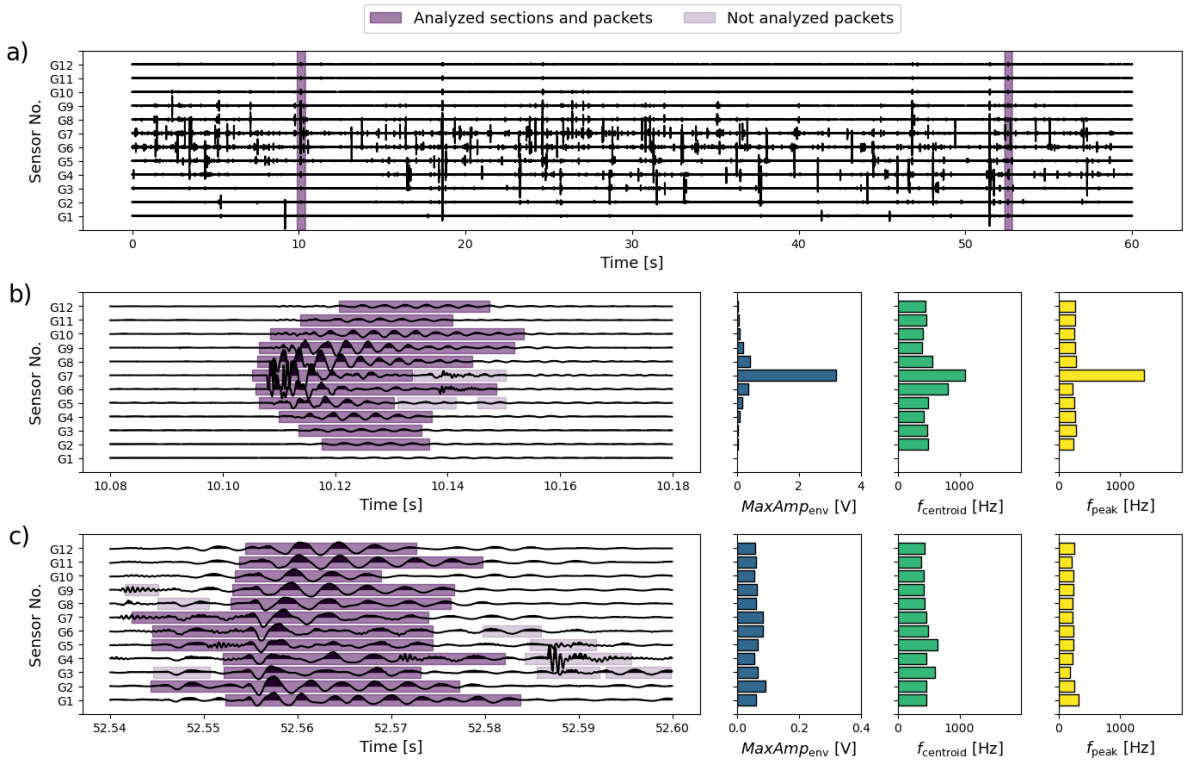

Figure 4. (**a**) Raw signal recorded by the 12 impact plates during a calibration measurement at the Navisence site (Table 2). The two purple stripes mark the time sections depicted in (**b**) and (**c**). Characterization of packets generated by (**b**) an impact on plate G7 and (**c**) an impact on the concrete sill close to the right bank. $MaxAmp_{env}$ is the maximum amplitude of the packet's envelope and $f_{centroid}$ and f_{peak} are the centroid and peak frequencies, respectively.

3.2 Characterization of Real and Apparent Packets

Results from the single-grain-size flume experiments conducted with the partition wall show that the number of packets recorded by the non-impacted plate (G1) increases together with the particle size (Table 3, Figure 5). While particles of the three smallest classes remained undetected by G1, the largest particles (j = 10) generated almost as many packets on G1 as on G2. Also note that the number of recorded packets per particle (α_{tot}) increases for both sensors with increasing $D_{m,j}$ (Table 3). α_{tot} values larger than 1 signify that multiple impacts are being identified per particle. With increasing particle size, the maximum centroid frequency of

packets decreases and the maximum amplitude increases (Figure 5), consistent with the Hertz contact theory (Barrière et al., 2015). In general, the packets detected by G1 appear to have lower amplitude and frequency values than those recorded by G2. Still, the packet characteristics of the two sensors overlap over a significant area of the amplitude-frequency plots (Figure 5). With the help of video material, it was found that these overlapping packets originate from impacts on the concrete bed.

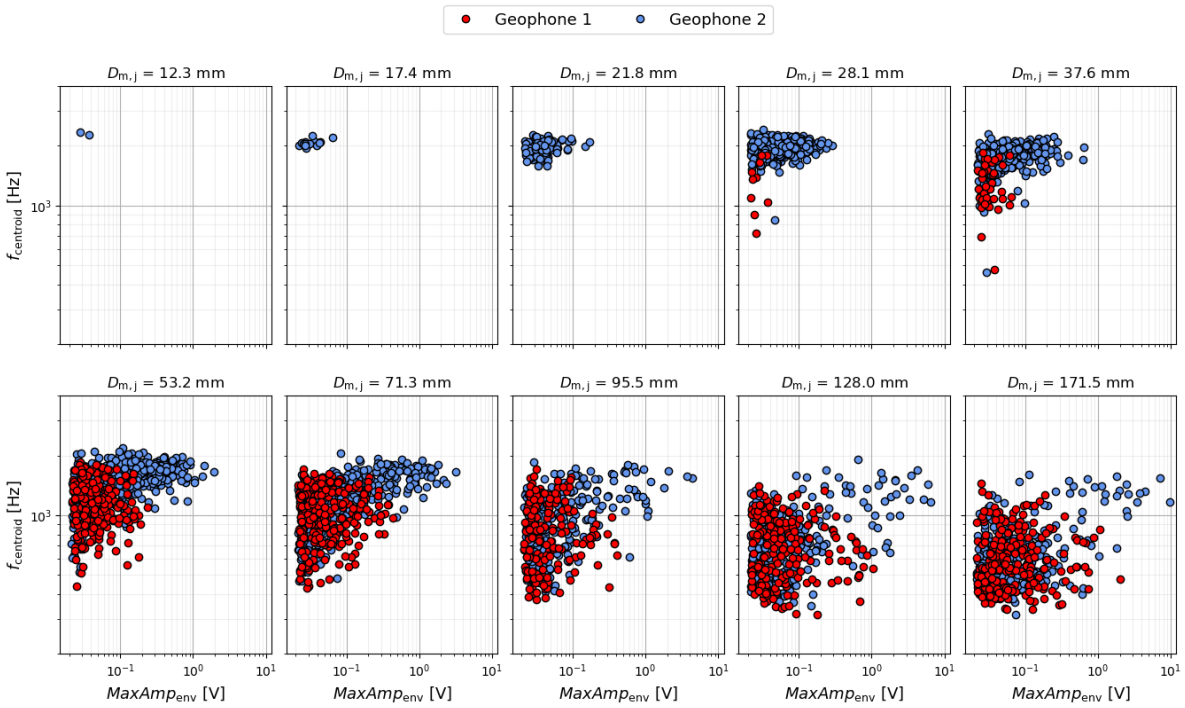

Figure 5. Amplitude and frequency characteristics of packets detected during the single-grain-size experiments conducted using the partition wall (Figure 2b). Each dot corresponds to one packet. The red and blue dots indicate packets recorded by the shielded plate (G1) and the un-shielded plate (G2), respectively.

Table 3. *Quantitative Evaluation of the Single-grain-size Experiments Conducted in the Modified Flume Set-up Including the Partition Wall (Figure 5)*

Grain-size class j	1	2	3	4	5	6	7	8	9	10
$D_{m,j}$	12.3	17.4	21.8	28.1	37.6	53.2	71.3	95.5	128	171.5
No. repetitions	5	5	5	7	5	5	5	5	5	4
N_j	500	500	400	462	200	200	125	50	25	23
$\alpha_{tot,G1}$	0	0	0	0.02	0.20	1.08	2.00	3.46	8.12	10.00
$\alpha_{tot,G2}$	0	0.03	0.27	0.89	1.43	2.30	2.99	4.80	10.44	12.30
$PACK_{G1}/PACK_{tot}$	0	0	0	0.02	0.12	0.32	0.40	0.42	0.44	0.45

Note. For each grain-size class *j*, the following information is listed: the mean particle diameter ($D_{m,j}$), the number of experimental runs (No. repetitions), the number of grains summed over all repetitions (N_j), the average number of recorded packets per particle by each sensor (α_{tot}), and the proportion of packets recorded by the shielded sensor G1 ($PACK_{G1}/PACK_{tot}$).

We now merge all the single-grain-size experiments conducted with the modified set-up to illustrate the packet characteristics for heterogeneous grain mixtures (under the assumption that any grain size interactions are minor). In Figure 6, we define real packets as packets recorded by the unshielded sensor (G2) that do not overlap with packets recorded by the shielded sensor (G1) in amplitude-frequency space. The three types of packet information listed in subsections 2.3.1-2.3.3 help to distinguish real from apparent packets. While $MaxAmp_{env,neighbor}$ and $f_{centroid}$ are efficient criteria over the whole range of $MaxAmp_{env}$ values (Figures 6a and 6b), f_{peak} shows more overlap between G1 and G2 packets for lower $MaxAmp_{env}$ values, and returns stable high frequency values over a large range of $MaxAmp_{env}$ values (Figure 6c).

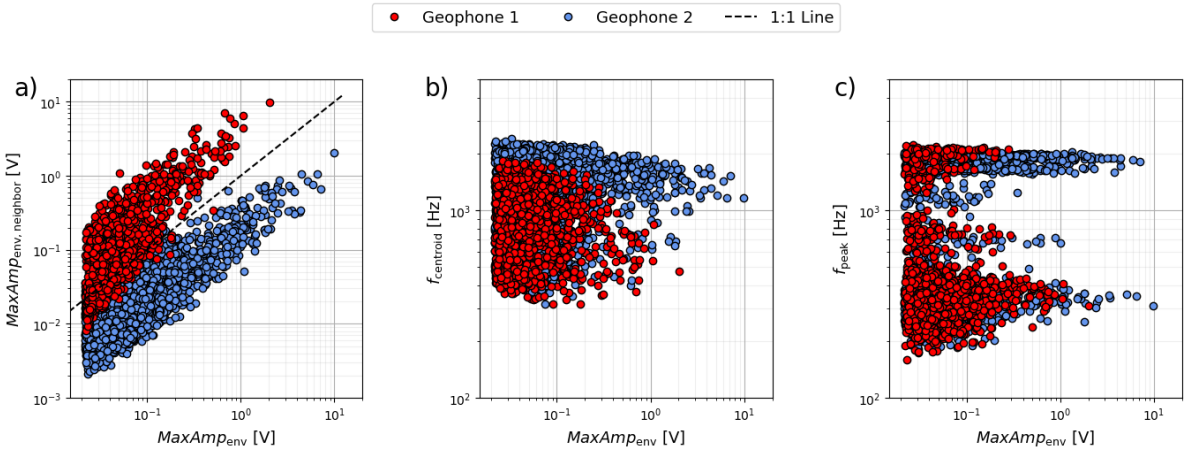

Figure 6. Illustration of all three packet attributes implemented in the filter method after having merged the single-grain-size experiments that used the partition wall (Figure 5). The panels show the relationships between the maximum amplitude of each packet's envelope $MaxAmp_{env}$ and (**a**) the maximum amplitude of the envelope of the closest neighboring sensor plates $MaxAmp_{env,neighbor}$, (**b**) the centroid frequency $f_{centroid}$ and (**c**) the peak frequency f_{peak}. Note that points lying on the 1:1 line in (**a**) correspond to packets having the same maximum amplitude in the two sensors.

To extrapolate the filter to field data, the signal responses of SPG systems in the field need to be similar to the signal response observed during the flume experiments. This can be examined using density histograms of the three types of packet information. In general, $f_{centroid}$

(Figure 7a.2-7e.2) and f_{peak} values (Figure 7a.3-7e.3) recorded during the flume experiments correlate well with the field data. In contrast, the $MaxAmp_{env,neighbor}$ values from the field data are more scattered than the values from the flume (Figure 7a.1-7e.1). The increased scatter is caused by the Erlenbach data. There, the propagating signal appears to be more strongly attenuated, which leads to larger differences between $MaxAmp_{env}$ and $MaxAmp_{env,neighbor}$.

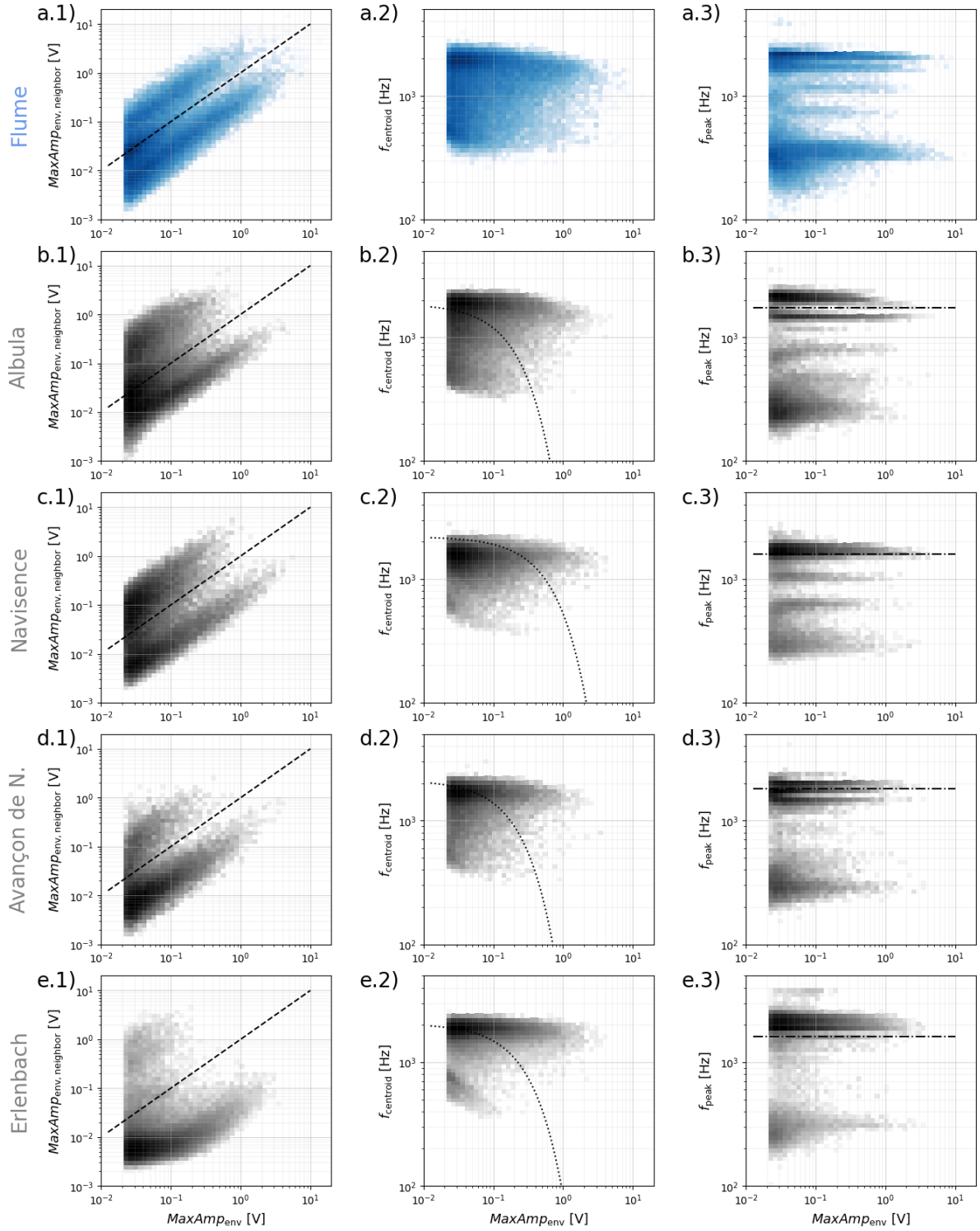

Figure 7. Density histograms of all three packet attributes implemented in the filter method using a resolution of 50x50 bins. The panels (**a.1-a.3**) show the amplitude and frequency information for all the packets detected during single-grain-size flume experiments, without the partition wall, reproducing the Albula, the Navisence and the Avançon de Nant field sites (Nicollier et al., 2021). The same amplitude and frequency information is shown for the field calibration measurements conducted at the Albula (**b.1-b.3**), the Navisence (**c.1-c.3**), the Avançon de Nant (**d.1-d.3**), and the Erlenbach site (**e.1-e.3**). Each dashed line in the panels of the first column (**a.1-e.1**) is the 1:1 line. Each dotted line in the panels of the second column (**b.2-e.2**) illustrates the f_{centroid} threshold derived for the given station (Table 4). Each dash-dotted line in the panels of the third column (**b.3-e.3**) illustrates the f_{peak} threshold derived for the given station (Table 4).

3.3 Filter Parameters

By taking the findings presented in the previous section into consideration, we can now design the filter. Each packet recorded by an impact plate is classified as "real" if either of two criteria applies. The first criterion is that the maximum amplitude recorded on one plate exceeds the maximum amplitude on both adjacent plates by a factor p_1, and the centroid frequency exceeds a specified exponential function of the maximum amplitude (because both will vary with the size of the impacting particle):

Criterion 1: $$MaxAmp_{\text{env}} > p_1 \cdot MaxAmp_{\text{env,neighbor}} \;\&\; f_{\text{centroid}} > lin_{\text{coeff}} \cdot e^{(exp_{\text{coeff}} \cdot MaxAmp_{\text{env}})}$$

The second criterion is that the maximum amplitudes recorded on one plate exceeds the maximum amplitude on both adjacent plates by a different factor p_2, and the peak frequency exceeds a value p_3:

Criterion 2: $$MaxAmp_{\text{env}} > p_2 \cdot MaxAmp_{\text{env,neighbor}} \;\&\; f_{\text{peak}} > p_3$$

The best values for the filter coefficients p_1, p_2, p_3, lin_{coeff} and exp_{coeff} (Table 4) were defined for various station configurations after multiple runs of the basin-hopping algorithm (as described in section 2.3) optimizing the coefficient of determination R^2 of Equation 2. The value of coefficient p_1 was constrained to be greater than or equal to 1, to ensure that *Criterion 1* excludes packets resulting from impacts on neighboring plates. The f_{centroid} threshold was set as an exponential function in order to best reproduce the boundary line between the domain where G1 and G2 packets overlap in Figure 6b, and the domain where they do not. The value of coefficient p_2 in *Criterion 2* is constrained to be less than 1 in order to accommodate some ambiguity in the recorded amplitudes, thus facilitating the

544 classification of impacts with less marked signatures, e.g. impacts close to the edge of a plate.
545 An illustration of the frequency thresholds can be found in Figure 7b.2-e.2 and 7b.3-e.3.
546
547 **Table 4.** *List of the Best Filter Coefficients*

	Criterion 1			Criterion 2	
Stations	p_1	lin_{coeff}	exp_{coeff}	p_2	p_3
Albula	1.56	1867	-4.51	0.31	1728
Navisence	1.33	2196	-1.43	0.31	1593
Avançon de Nant	1.43	2123	-4.28	0.74	1817
Erlenbach	1.48	2046	-3.19	0.77	1611
3 stations [a]	1.57	2017	-2.92	0.35	1616
4 stations [b]	1.75	2390	-3.44	0.37	1662

548 *Note.* The filter coefficients p_1, p_2, p_3, lin_{coeff} *and* exp_{coeff} were estimated by using the basin-hopping
549 algorithm to optimize the coefficient of determination R^2 of Equation 2 for various station
550 configurations.
551 [a] Includes the following three stations : Albula, Navisence and Avançon de Nant
552 [b] Includes the following four stations : Albula, Navisence , Avançon de Nant and Erlenbach

553 ### 3.4 Filtering Flume and Field Data

554 Figure 8 shows the application of the calibrated filter to the time series shown in Figure 3.
555 One can notice that the two real packets originating from direct impacts on plate G2 (between
556 0.08 and 0.11 seconds) and plate G1 (between 0.17 and 0.19 seconds) have been successfully
557 identified (Figure 8a and b). Additionally, packet pairs generated by impacts on the concrete
558 were correctly classified as “apparent”. Applying the filter to the raw signals recorded during
559 all of the single-grain-size flume experiments (without the partition wall) provides further
560 information on the number of apparent packets generated by each grain-size class. The mean
561 α_{tot} values, i.e. the number of packets generated by a single particle, for both unfiltered and
562 filtered data, begin to diverge at class j = 4 (Figure 8c). This is consistent with the findings
563 from the partition wall flume experiments (Figure 5). Note that for size classes j = 9 and 10,
564 less than 10% of the packets remain after filtering, implying that over 90% of the packets
565 generated by these size classes are "apparent" rather than real. Interestingly, the filtering
566 process results in a relatively stable signal response over the grain-size classes j = 4 to 10,
567 with $\alpha_{tot,real}$ values ranging from 0.78 to 1.68. Before the filter was applied, $\alpha_{tot,all}$ varied by
568 more than a factor of 15, ranging from 1.1 to 18 for the same seven grain-size classes.

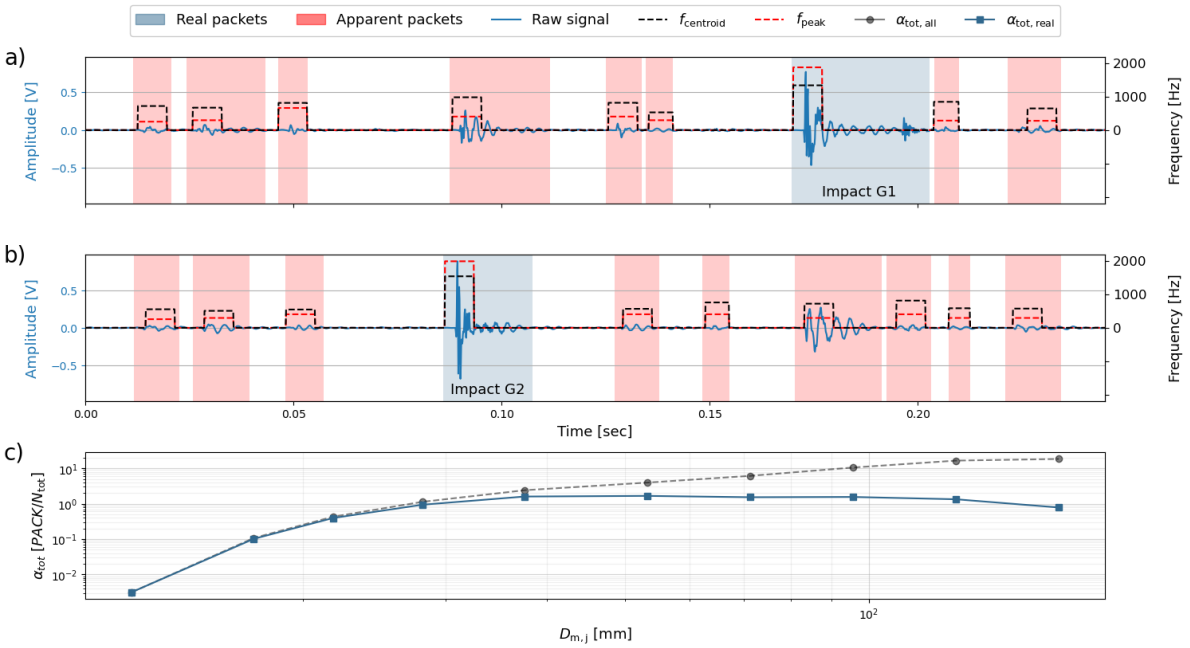

Figure 8. Raw signal recorded by the impact plates (**a**) G1 and (**b**) G2 during a single-grain-size flume experiment with particles of class j = 6. This figure corresponds to Figure 3, but after the application of the filter based on all 4 stations (Table 4). Real packets are marked in blue and apparent packets are marked in red. (**c**) shows the change of the α_{tot} value from before (dashed grey line, $\alpha_{tot,all}$) to after filtering (solid blue line, $\alpha_{tot,real}$) as function of the mean particle diameter $D_{m,j}$. Here α_{tot} was calculated from the mean value over all the single-grain-size flume experiments reproducing the Albula, the Navisence and the Avançon de Nant field sites for a given grain size j.

Finally, we apply the filter to the calibration data from the four field sites, using the optimal parameters listed in Table 4. While the power-law regression lines fit the data better (Figure 9), the linear relations are useful to evaluate the effect of the filtering, and thus Table 5 includes both linear and power-law coefficients. The following observations can be made: First, through filtering, 48 to 57 % of the packets recorded at the Albula, Navisence and Avançon de Nant sites were removed (i.e. identified as apparent packets). At the Erlenbach site, only 20 % of the packets were removed. Second, as the example of the Albula dataset shows, filtering may not necessarily improve the calibration relation at individual stations. Third, after application of the filter, the Erlenbach station still records about two times fewer packets than the other stations for a given bedload flux. Last, (iv) filtering improves the coefficient of determination R^2 of the global calibration relation valid for all four sites from 0.80 to 0.91.

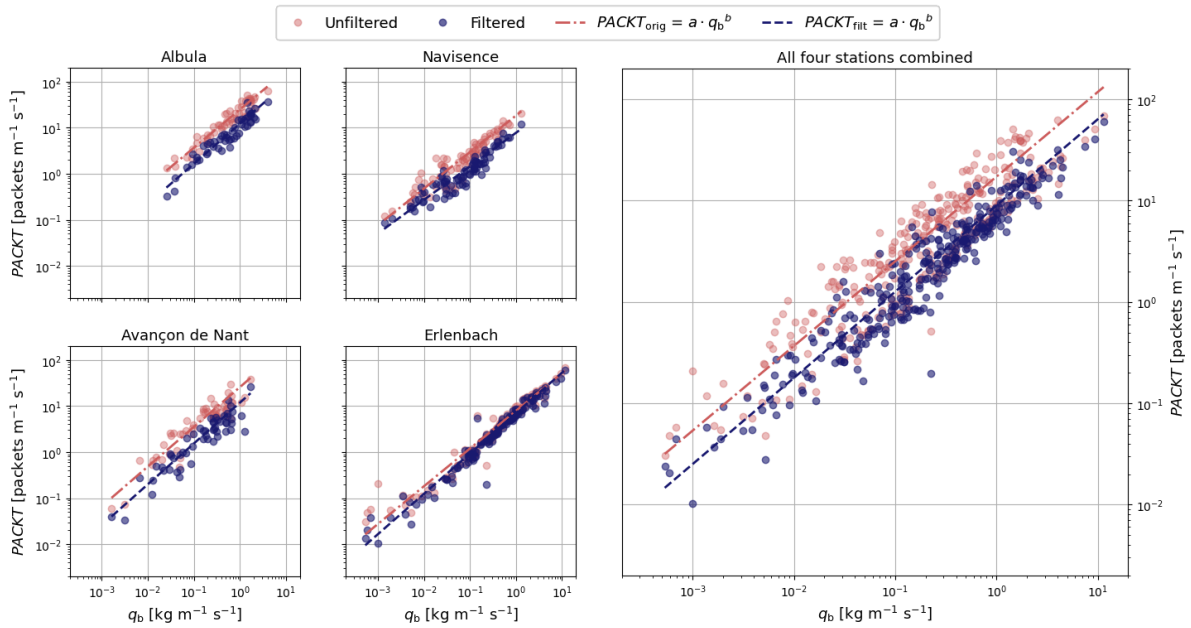

Figure 9. Total flux calibration relations linking the packet rate *PACKT* to the unit transport rate q_b before (red) and after filtering (blue). Each dot corresponds to one calibration measurement. The dashed lines are power-law regression lines (Equation 2); their coefficients are listed in Table 5. The filtered data was obtained using the optimal filter coefficients listed in Table 3.

Table 5: *The Coefficients a and b of the Power-law and Linear least-squares Regression Equations (Equation 2) for Different Field Sites Combinations.*

		Unfiltered			Filtered		
	Field Sites	*a*	*b*	R^2	*a*	*b*	R^2
Power-law	Albula	24.81	0.83	0.93	12.21	0.87	0.91
	Navisence	18.35	0.79	0.86	7.76	0.73	0.88
	Avançon de Nant	25.69	0.86	0.86	11.82	0.89	0.86
	Erlenbach	7.89	0.82	0.94	7.04	0.88	0.96
	3 stations [a]	24.20	0.86	0.90	11.46	0.84	0.89
	4 stations [b]	17.21	0.84	0.80	8.94	0.85	0.91
Linear Least-squares	Albula	28.73	1	0.87	13.65	1	0.87
	Navisence	34.92	1	0.74	18.26	1	0.67
	Avançon de Nant	35.40	1	0.80	15.35	1	0.82
	Erlenbach	10.90	1	0.88	8.62	1	0.93
	3 stations [a]	33.18	1	0.86	16.75	1	0.82
	4 stations [b]	24.93	1	0.71	12.23	1	0.85

Note. The corresponding coefficients of determination R^2 are also listed. The "filtered" coefficients were obtained from data filtered using the optimal filter parameters listed in Table 4.

[a] Includes the following three stations : Albula, Navisence and Avançon de Nant

[b] Includes the following four stations : Albula, Navisence, Avançon de Nant and Erlenbach

4 Discussion

4.1 Purpose of Filtering

The reasons for the six-fold site-to-site variation in the linear calibration coefficients linking geophone signals to the transported bedload (e.g. Rickenmann et al., 2014; Rickenmann & Fritschi, 2017) are gradually becoming clearer. Wyss et al. (2016b) found that in flume experiments, higher flow velocities result in fewer packets per unit mass being recorded, due to longer saltation lengths and flatter impact angles. Another important factor influencing the signal response was found to be the grain-size distribution (GSD) of the transported bedload (Nicollier et al., 2021). By comparing results from field and flume calibration measurements, Nicollier et al. (2021) found that the coarser a grain mixture is, the more packets are recorded by the SPG system per unit weight, mainly in the four smallest amplitude classes. The findings presented in the present study support the hypothesis that the effect of the GSD on the signal response is related to the phenomenon of wave propagation. The field data presented here demonstrate that strong impacts can generate seismic waves that propagate far enough to be detected by multiple sensors (Figure 4). Consequently, the coarser the mobilized bedload is, the more packets are being generated by waves propagating from outside an individual plate. Unfortunately the GSD will typically be unknown in a given stream, unless bedload samples are collected or unless it can be inferred from the SPG signals themselves (which is the subject of an upcoming paper, currently in preparation). A further complication is that the GSD effect on the signal response varies with the station's geometry. The wider a monitored transect is and the more plates are installed, the more apparent packets will be recorded for a given bedload mass. At the Erlenbach, almost all of the bedload is carried over only two plates because of the convex shape of the artificial stream bed. At the other sites, bedload transport is distributed over 10 to 30 plates (Table 2). Additionally, the samples collected at the Erlenbach generally have a finer GSD than at the other three sites. Finally, the flow velocity V_w at the Erlenbach is 1.6 to 3.8 times higher than at the other sites (Table 2). These differences in geometry, GSD and flow velocity may explain why the Erlenbach station records about three times fewer packets per unit mass than the three other stations, before the filter is applied (Table 5).

The filter method described in this study functions as an insulator that decouples each plate from its surroundings and thus suppresses seismic waves generated outside of the plate boundaries. The advantage of filtering is twofold: (i) it attenuates the effect of the station's geometry and the GSD on the signal response, and (ii) the remaining site-dependent factors

637 that influence SPG signals are all measurable quantities, such as the flow velocity, the bed
638 slope or the bed roughness.

639 **4.2 Field- and Flume-based Identification of Propagating Waves**

640 Two sources of apparent packets were identified: (i) impacts on a neighboring plate and (ii)
641 impacts on the surrounding concrete bed. In Figures 3 and 4, it was shown that each source
642 has a different seismic signature. An impact on a plate generates a wave with attributes that
643 vary systematically as it propagates along the array of sensors, i.e. the amplitude decreases
644 and the high frequencies are progressively attenuated. By contrast, an impact on the concrete
645 bed generates packets with similar attributes at multiple sensors. The travel path followed by
646 the waves could be a possible explanation for these distinct signatures. For an impact on
647 concrete, the wave is only slightly attenuated by the dense concrete and then propagates
648 through similar amounts of steel and elastomer at all sensor plates. This would explain the
649 similarities in the recorded waveforms, with the only major differences between the detected
650 packets being their start times (Figure 4c). In the case of an impact on a plate, we hypothesize
651 that the wave is strongly attenuated along its lateral travel path from sensor to sensor, as it
652 repeatedly crosses the soft elastomer layer (Figure 4b).
653
654 Even though the propagation of the seismic waves is clearly visible in the field data (Figure
655 4), investigating their origin required flume experiments. Thanks to the video material
656 recorded during each of these experiments, we were able to draw links between the signal
657 response of the SPG system and the impact location. The installation of a partition wall
658 provided a simple but efficient way to shield one plate from direct impacts and investigate the
659 origins of "apparent" packets. In Figures 5 and 6, impacts on the concrete are shown to
660 generate overlapping packet characteristics at plates G1 and G2; thus isolating the plates from
661 each other with elastomer is not sufficient to avoid the recording of apparent packets. The
662 flume set-up was designed to replicate the flow and transport conditions during the field
663 campaigns, including the transport of natural bedload particles (Nicollier et al., 2021). This
664 possibly explains the good correlation between the flume and field-based density histograms
665 of the three packet attributes used in the filter (Figure 7). Because the optimization process
666 used to find the best filter coefficients is based only on the field data, a perfect match between
667 the flume and field data is not required.
668

669 ### 4.3 Filter Design

670 We have shown that in order to isolate an individual plate, we must decouple it from the other
671 plates and from the concrete bed. Our proposed filter attempts to perform this decoupling
672 using only amplitude and frequency information, for two main reasons. First, the flume
673 experiments with the partition wall showed that this information can be used to distinguish
674 real from apparent packets (Figures 5 and 6). Second, extracting this information from the
675 packets is computationally efficient, which is crucial to avoid any data loss from overloading
676 the buffer memory.
677
678 The filter was designed to encompass most impact situations. *Criterion 1*, with its amplitude-
679 ratio coefficient p_1 of around 1.5 and its exponential $f_{centroid}$ threshold line (Table 4, Figure
680 7b.2-7e.2), identifies the most obvious real packets. *Criterion 2* is meant as a complementary
681 filter element that classifies packets with less distinct characteristics. These could be packets
682 generated by impacts on the concrete, often resulting in a $MaxAmp_{env}$-$MaxAmp_{env,neighbor}$ ratio
683 close to 1 and low f_{peak} values. Furthermore, due to the stochastic nature of bedload transport,
684 a particle can impact onto any point on a plate (Turowski et al., 2013). Particles impacting
685 close to a neighboring plate will often yield $MaxAmp_{env}$-$MaxAmp_{env,neighbor}$ ratios close to 1,
686 making it difficult to correctly classify the resulting packets. However, in this case, the f_{peak}
687 value recorded by the impacted plate often remains larger than for the neighboring plate due
688 to the damping effect of the elastomer layer. Finally, *Criterion 2* also covers the few cases
689 where the real packet has a $MaxAmp_{env}$-$MaxAmp_{env,neighbor}$ ratio lower than 1 but a high
690 frequency content, e.g. when two distinct particles impact close enough in time on two
691 different plates.
692
693 The general structure of the filter was defined on the basis of the results from the flume
694 experiments that included the partition wall (Figure 6). However, the optimal coefficients
695 were derived using field data only, in order to account for site-to-site differences in flow and
696 transport conditions as well as station geometries. These site-specific characteristics could
697 explain the (limited) variability in the coefficients listed in Table 4. But given the wide ranges
698 covered by the frequency attributes, the f_{peak} and $f_{centroid}$ thresholds differ only slightly from
699 each other. Another encouraging result is that the optimized $f_{centroid}$ threshold lines shown in
700 Figure 7b.2-e.2 approximately follow the upper border of the apparent packets' characteristics
701 for G1 in Figure 6b.
702

4.4 Application of the Filter to Field and Flume Data

Before addressing the results from the filtering of field and flume data, it is necessary to go back one step and discuss the meaning of the calibration. Whether we calibrate a SPG system installed at a field site or in the flume, the procedure is the same. Using Equation 2, we relate the number of detected packets to the bedload mass that was either sampled with the basket or transported in the flume over a given time interval. Additionally, we can use the α_{tot} coefficient (Equation 3) to define the detectability of particles. The more packets that are being recorded per sampled particle (in the field data) or per fed particle (in the flume experiments), the more accurate the calibration will be. Including apparent packets in the calibration will therefore influence the calibration relationship for a given station, but not necessarily reduce its accuracy. The α_{tot} values observed for the single-grain size experiments after filtering (Figure 8c) suggest that filtering roughly equalizes the detectability of the seven largest particle classes, with unfiltered data yielding greater numbers of "apparent" packets as particle size increases. Two further observations support the coherence of the filter method. First, the differences between $\alpha_{tot,all}$ and $\alpha_{tot,real}$ in Figure 8c correlate with the $PACK_{G1}/PACK_{tot}$ ratios in Table 3, i.e., the classes for which filtering strongly reduced the number of packets were also the classes that yielded many apparent packets in the flume experiments using the partition wall. Second, the site-specific calibration R^2 values in Table 5 changed only slightly after the filter was applied, even though doing so removed half of the packets.

The main purpose of the filter is to diminish the effect of the station geometry on the signal response. The comparison of the linear coefficient *a* for the stations listed in Table 5 shows that removing apparent packets significantly reduces the differences among the site-specific calibration relationships. However, after filtering, the Erlenbach station still records fewer packets per unit mass than the other three sites. The following factors could explain this. First, the high flow velocity V_w measured at the Erlenbach, potentially allowing more particles to hop over the array of SPG plates than at the other sites (see Subsection 4.1). Second, after having noticed the site-to-site differences visible in Figure 7b.1-e.1, we computed the mean $MaxAmp_{env}$-$MaxAmp_{env,neighbor}$ ratio for each station, obtaining 4.0 for the Albula, 4.2 for the Navisence, 4.8 for the Avançon de Nant and 9.3 for the Erlenbach. This result suggests that the plates at the Erlenbach are particularly well isolated from their surroundings. Note that the Erlenbach station is equipped with the first version of the SPG system, which differs slightly from the SPG system installed at the other sites, i.e. the watertight casing for the geophone and the type and positioning of the screws holding the plate are somewhat different. Third, it

737 is probable that the filtering process does not eliminate all the apparent packets. However, this
738 would have only a limited impact at the Erlenbach station, which is, as we have seen, already
739 less prone to recording apparent packets for multiple reasons.
740
741 The most encouraging result from the filtering is certainly the improvement of the coefficient
742 of determination R^2 of the global calibration relationship valid across all four sites from 0.80
743 to 0.91. Applying an individual filter to each site also reduces the variability of the *a*
744 coefficient for linear calibrations (b = 1), with *a* varying by a factor of only 2.1 (Table 5). We
745 can therefore conclude that (i) "apparent" packets arise primarily from seismic wave
746 propagation, (ii) filtering out these "apparent" packets yields improves estimates of bedload
747 transport rates, and (iii) because the effects of seismic wave propagation vary among SPG
748 sites, the most effective filters will be those that are based on site-specific calibrations.

749 **5 Conclusion**

750 The Swiss plate geophone (SPG) is a bedload surrogate monitoring system that has been
751 installed in several gravel bed streams and calibrated using direct sampling techniques. In this
752 study, video recordings of controlled flume experiments and raw data recorded at bedload
753 monitoring stations in the field both confirm the findings from Antoniazza et al. (2020) that
754 the SPG system is biased by acoustic waves propagating through the apparatus. These waves
755 were found to originate from particles impacting on the surrounding concrete sill or on
756 neighboring plates. Flume setups replicated natural transport conditions, but with the addition
757 of a partition wall to shield one plate from impacts. Single-grain-size experiments were
758 performed to characterize the "apparent" packets, i.e. packets generated by impacts occurring
759 beyond an individual plate, and to design a filter that identifies and removes these packets.
760 The experiments confirmed that larger particles generated larger numbers of apparent packets.
761 Amplitude and frequency patterns arising from the flume experiments suggest that packet
762 characteristics can be used to distinguish real from apparent packets. The findings of these
763 single-grain-size flume experiments were used to design a filter method, which was
764 subsequently optimized using field data. Applying this filter results in more consistent
765 calibration relationships among the different sites, and facilitates the derivation of a single
766 calibration relationship that yields reasonable estimates of bedload transport rates at all four of
767 our field sites. These findings suggest that the filter method could also potentially improve
768 estimates of fractional transport rates, particularly for the smaller grain-size fractions.
769 Acoustic waves are attenuated by their propagation through an SPG installation, so apparent
770 packets will mostly have small amplitudes that would be mistakenly attributed to small

771 particles. Removing these apparent packets could therefore improve SPG estimates of
772 transport rates for smaller size fractions in grain-size mixtures. Removing apparent packets
773 also clarifies how site-specific factors (e.g., flow velocity, bed slope, and bed roughness)
774 influence transport rate estimates from SPG systems. Preliminary results also suggest that this
775 filter may improve estimates of the spatial distribution of bedload transport along transects of
776 SPG plates. In the future, packet classification based on this filter could be used to build a
777 labeled data set on which machine learning algorithms could be trained potentially further
778 improving the transport estimates. More generally, this study highlights the importance of
779 insulating sensors as much as possible from surrounding noise sources, or correcting for the
780 resulting signal contamination.

781 **Acknowledgements**

782 This study was supported by the Swiss National Science Foundation (SNSF), grant
783 200021L_172606, and by the Deutsche Forschungsgemeinschaft (DFG), grant RU 1546/7-1.
784 The authors warmly thank Norina Andres, Mehdi Mattou, Nicolas Steeb, Florian Schläfli,
785 Konrad Eppel and Jonas von Wartburg for their great help during the field calibration
786 campaigns. They are also grateful to Michael Herkenroth of the TU Munich and the whole
787 staff of the Oskar von Miller Institute for helping to set up and perform the flume
788 experiments. Lorenz Ammann and Alexandre Badoux are further thanked for their valuable
789 suggestions regarding an earlier version of the manuscript. The authors declare no conflict of
790 interest. All data presented in this paper is available online on the EnviDat repository
791 https://www.envidat.ch/#/metadata/sediment-transport-observations-in-swiss-mountain-
792 streams.

References

Ammon, C. J., Velasco, A. A., Thorne Lay, T., Wallace, T. C. (2021). An overview of earthquake and seismic-wave mechanics, Editor(s): Ammon, C. J., Velasco, A. A., Thorne Lay, T., Wallace, T. C. (Eds.), *Foundations of Modern Global Seismology, 2*, 39-63, Academic Press. https://doi.org/10.1016/B978-0-12-815679-7.00009-4.

Ancey, C. (2020). Bedload transport: a walk between randomness and determinism. Part 2. Challenges and prospects. *Journal of Hydraulic Research*, 58, 18-33. https://doi.org/10.1080/00221686.2019.1702595

Antoniazza, G., Nicollier, T., Wyss, C. R., Boss, S., & Rickenmann, D. (2020). Bedload transport monitoring in alpine rivers: Variability in Swiss plate geophone response. Sensors, *20*. https://doi.org/10.3390/s20154089

Badoux, A., Peter, A.,Rickenmann, D., Junker, J.,Heimann, F., Zappa, M., & Turowski, J. M. (2014). Geschiebetransport und Forellenhabitate in Gebirgsflüssen der Schweiz: mögliche Auswirkungen der Klimaänderung. *Wasser Energie Luft, 3/2014*. 200-209. Schweizerischer Wasserwirtschaftsverband. Baden.

Barrière, J., Krein, A. , Oth, A., & Schenkluhn, R. (2015). An advanced signal processing technique for deriving grain size information of bedload transport from impact plate vibration measurements, Earth Surf. Processes Landforms, doi:10.1002/esp.3693.

Benateau, S., Gaudard, A., Stamm, C., & Altermatt, F. (2019). Climate change and freshwater ecosystems: Impacts on water quality and ecological status. *Hydro-CH2018Project*. 110pp. Federal Office for the Environment (FOEN), Bern, Switzerland. https://doi.org/10.5167/uzh-169641

Blöschl, G., Kiss, A., Viglione, A., Barriendos, M., Böhm, O., Brázdil, R., et al. (2020). Current European flood-rich period exceptional compared with past 500 years. *Nature, 583*(7817). 560–566. https://doi.org/10.1038/s41586-020-2478-3

Bogen, J., & Møen, K. (2003). Bed load measurements with a new passive acoustic sensor, in Erosion and Sediment Transport Measurement in Rivers: Trends and Explanation. *IAHS Publications, 283*, 181-182.

821 Bunte, K., Abt, S. R., Potyondy, J. P., & Ryan, S. E. (2004). Measurement of coarse gravel
822 and cobble transport using a portable bedload trap. *Journal of Hydraulic Engineering*, *130*(9),
823 879-893. https://doi.org/10.1061/(ASCE)0733-9429(2004)130:9(879)

824 Camenen, B., Jaballah, M., Geay, T., Belleudy, P., Laronne, J. B., & Laskowski, J. P. (2012).
825 Tentative measurements of bedload transport in an energetic alpine gravel bed river. In River
826 Flow 2012, Muñoz RM (Ed.). CRC Press: Boca Raton, FL.

827 Choi, J. H., Jun, K. W., & Jang, C. D. (2020). Bed-Load Collision Sound Filtering through
828 Separation of Pipe Hydrophone Frequency Bands. *Water*, *12*, 1875.
829 https://doi.org/10.3390/w12071875

830 Conevski, S., Winterscheid, A., Ruther, N., Guerrero, M., & Rennie, C. (2018). Evaluation of
831 an acoustic Doppler technique for bed-load transport measurements in sand-bed Rivers. *E3S*
832 *Web of Conferences*, *40*, 02053. https://doi.org/10.1051/e3sconf/20184002053

833 Dell'Agnese, A., Mao, L., Comiti, F. (2014). Calibration of an acoustic pipe sensor through
834 bedload traps in a glacierized basin, *CATENA*, *121*, 222-231.
835 https://doi.org/10.1016/j.catena.2014.05.021

836 Dietze, M., Lagarde, S., Halfi, E., Laronne, J. B., & Turowski J.M. (2019). Joint sensing of
837 bedload flux and water depth by seismic data inversion. *Water Resources Research, 55*,
838 9892– 9904. https://doi.org/10.1029/2019WR026072

839 Einstein, H. A. (1937). The Bedload Transport as Probability Problem. *Mitteilung der*
840 *Versuchsanstalt für Wasserbau an der Eidgenössischen Technischen Hochschule*, Zürich,
841 Switzerland.

842 Ferguson, R. I. (1986). River Loads Underestimated by Rating Curves. *Water Resources*
843 *Research*, *22*, 74-76. https://doi.org/10.1029/WR022i001p00074

844 FOEN (ed.). (2021). Effects of climate change on Swiss water bodies. Hydrology, water
845 ecology and water management. *Environmental Studies.* (No. 2101). 125p. Federal Office for
846 the Environment FOEN, Bern, Switzerland.

847 Geay, T., Belleudy, P., Gervaise, C., Habersack, H., Aigner, J., Kreisler, A., et al. (2017).
848 Passive acoustic monitoring of bedload discharge in a large gravel bed river: Acoustic
849 monitoring of bedload transport. *Journal of Geophysical Research: Earth Surface*, *122*.
850 https://doi.org/10.1002/2016JF004112

851 Geay, T., Zanker, S., Misset, C., & Recking, A., (2020). Passive Acoustic Measurement of
852 Bedload Transport: Toward a Global Calibration Curve? *Journal of Geophysical Research:*
853 *Earth Surface*, *125*. https://doi.org/10.1029/2019JF005242

854 Gimbert, F., Fuller, B. M., Lamb, M. P., Tsai, V. C., & Johnson, J. P. L. (2019). Particle
855 transport mechanics and induced seismic noise in steep flume experiments with
856 accelerometer-embedded tracers. *Earth Surface Processes and Landforms*, *44*, 219-241.
857 https://doi.org/10.1002/esp.4495

858 Goupillaud, P., Grossmann, A., & Morlet, J. (1984). Cycle - Octave and Related Transforms
859 in Seismic Signal Analysis. *Geoexploration*, *23*, 85-102.

860 Gray, J. R., Laronne, J. B., Marr, J. D. G. (eds). (2010). Bedload-surrogate Monitoring
861 Technologies, *US Geological Survey Scientific Investigations Report, 2010–5091*. US
862 Geological Survey: Reston, VA. http://pubs.usgs. gov/sir/2010/5091/

863 Habersack, H., Seitz, H., & Laronne, J.B. (2008). Spatio-temporal variability of bedload
864 transport rate: analysis and 2D modelling approach. *Geodinamica Acta*, *21*(1-2), 67-79.
865 https://doi.org/10.3166/ga.21.67-79

866 Habersack, H., Kreisler, A., Rindler, R., Aigner, J., Seitz, H., Liedermann, M., & Laronne, J.
867 B. (2017). Integrated automatic and continuous bedload monitoring in gravel bed rivers.
868 *Geomorphology*, *291*, 80–93. https://doi.org/10.1016/j.geomorph.2016.10.020

869 Harper, W. V. (2014). Reduced Major Axis Regression: Teaching Alternatives to Least
870 Squares. *Mathematics Faculty Scholarship*, *24*.
871 https://digitalcommons.otterbein.edu/math_fac/24

872 Helley, E. J., & Smith, W. (1971). Development and calibration of a pressure-difference
873 bedload sampler. US Department of the Interior, Geological Survey, Water Resources
874 Division.

875 Hilldale, R. C., Carpenter, W. O., Goodwiller, B., Chambers, J. P. and Randle, T. J. (2015).
876 Installation of impact plates to continuously measure bed load: Elwha River, Washington,
877 USA. *Journal of Hydraulic Engineering*. *141*(3). https://doi.org/10.1061/(ASCE)HY.1943-
878 7900.0000975
879

Hirschberg, J., Fatichi, S., Bennett, G. L., McArdell, B. W., Peleg, N., Lane, S. N., et al. (2021). Climate change impacts on sediment yield and debris-flow activity in an Alpine catchment. *Journal of Geophysical Research: Earth Surface*, *126*, e2020JF005739. https://doi.org/10.1029/2020JF005739

Johnson, K. (1985). Contact Mechanics. Cambridge: Cambridge University Press. https://doi.org/10.1017/CBO9781139171731

Jones, E., Oliphant, T., & Peterson, P. (2002). SciPy: Open source scientific tools for Python [Cited 2021 June 16]. Available from: http://www.scipy.org

Koshiba , T., & Sumi, T. (2018). Application of the wavelet transform to sediment grain sizes analysis with an impact plate for bedload monitoring in sediment bypass tunnels. *E3S Web of Conferences*, *40*, 04022, https://doi.org/10.1051/e3sconf/20184004022

Koshiba, T., Auel, C., Tsutsumi, D., Kantoush, S. A., & Sumi, T. (2018). Application of an impact plate – Bedload transport measuring system for high-speed flows. *International Journal of Sediment Research*, *33*. https://doi.org/10.1016/j.ijsrc.2017.12.003

Krein, A., Klinck, H., Eiden, M., Symader, W., Bierl, R., Hoffmann, L., & Pfister, L. (2008). Investigating the transport dynamics and the properties of bedload material with a hydro-acoustic measuring system. *Earth Surface Processes and Landforms*, 33, 152–163. https://doi.org/10.1002/esp.1576

Kreisler, A., Moser, M., Aigner, J., Rindler, R., Tritthard, M., & Habersack, H. (2017). Analysis and classification of bedload transport events with variable process characteristics. *Geomorphology, 291*, 57–68. https://doi.org/10.1016/j.geomorph.2016.06.033

Kristeková, M., Kristek, J., Moczo, P., & Day, S. M. (2006). Misfit Criteria for Quantitative Comparison of Seismograms. *Bulletin of the Seismological Society of America*, *96*(5), 1836–1850. https://doi.org/10.1785/0120060012

Kuhnle, R., Wren, D., Hilldale, R. C., Goodwiller, B., & Carpenter, W. (2017). Laboratory Calibration of Impact Plates for Measuring Gravel Bed Load Size and Mass. *Journal of Hydraulic Engineering*, *143*. https://doi.org/10.1061/(ASCE)HY.1943-7900.0001391

Le Guern, J., Rodrigues, S., Geay, T., Zanker, S., Hauet, A., Tassi, P., et al. (2021). Relevance of acoustic methods to quantify bedload transport and bedform dynamics in a large sandy-gravel-bed river, *Earth Surface Dynamics, 9*, 423–444. https://doi.org/10.5194/esurf-9-423-2021.

Mao, L., Carrillo, R., Escauriaza, C., & Iroume, A. (2016). Flume and field-based calibration of surrogate sensors for monitoring bedload transport. *Geomorphology*, *253*, 10-21. https://doi.org/10.1016/j.geomorph.2015.10.002

Mizuyama, T., Laronne, J. B., Nonaka, M., Sawada, T., Satofuka, Y., Matsuoka, M., et al. (2010a) Calibration of a passive acoustic bedload monitoring system in Japanese mountain rivers. In Bedload-surrogate Monitoring Technologies, Gray, J. R., Laronne, J. B., Marr, J. D. G. (Eds.), *US Geological Survey Scientific Investigations Report, 2010–5091,* 296–318. US Geological Survey: Reston, VA. http://pubs.usgs.gov/sir/2010/5091/papers/listofpapers.html

Mizuyama, T., Oda, A., Laronne, J. B., Nonaka, M., & Matsuoka, M. (2010b). Laboratory tests of a Japanese pipe geophone for continuous acoustic monitoring of coarse bedload. In Bedload-surrogate Monitoring Technologies, Gray, J. R., Laronne, J. B., Marr, J. D. G. (Eds.), *US Geological Survey Scientific Investigations Report, 2010–5091,* 319–335. US Geological Survey: Reston, VA. http://pubs.usgs.gov/sir/2010/5091/papers/listofpapers.html

Mühlhofer, L. (1933). Untersuchungen über die Schwebstoff und Geschiebeführung des Inn nächst Kirchbichl (Tirol). *Die Wasserwirtschaft, 1*(6), 23 pp.

Nicollier, T., Rickenmann, D., & Hartlieb, A. (2019). Field calibration of the Swiss plate geophone system at the Albula stream and comparison with controlled flume experiments. 8 pp. Paper presented at the SEDHYD 2019 Conference, Reno, NV.

Nicollier, T., Rickenmann, D., Boss, S., Travaglini, E., & Hartlieb, A. (2020). Calibration of the Swiss plate geophone system at the Zinal field site with direct bedload samples and results from controlled flume experiments. In River Flow 2020. *Proceedings of the 10th Conference on Fluvial Hydraulics*, 901–909. https://doi.org/10.1201/b22619

Nicollier, T., Rickenmann, D., Hartlieb, A. (2021). Field and flume measurements with the impact plate: Effect of bedload grain-size distribution on signal response. *Earth Surface Processes and Landforms*, 17 pp. https://doi.org/10.1002/esp.5117

Raven, E. K., Lane, S. N., & Ferguson, R. (2010). Using sediment impact sensors to improve the morphological sediment budget approach for estimating bedload transport rates. *Geomorphology*, *119*, 125–134. https://doi.org/10.1016/j.geomorph.2010.03.012

Reid, I., Frostick, L. E., & Layman, J.T. (1985). The incidence and nature of bedload transport during flood flows in coarse-grained alluvial channels. *Earth Surface Processes and Landforms*, *10*, 33-44. https://doi.org/10.1002/esp.3290100107

Rickenmann, D. (2016), Bedload transport measurements with geophones, hydrophones and underwater microphones (passive acoustic methods), in Gravel Bed Rivers and Disasters, edited by D. Tsutsumi and J. B. Laronne, John Wiley, in press.

Rickenmann, D. (2017). Bed-load transport measurements with geophones and other passive acoustic methods. *Journal of Hydraulic Engineering*, *143*(6), 03117004-1-14. https://doi.org/10.1061/(ASCE)HY.1943-7900.0001300

Rickenmann, D., & McArdell, B. W. (2007). Continuous measurement of sediment transport in the Erlenbach stream using piezoelectric bedload impact sensors. *Earth Surface Processes and Landforms*, *32*(9), 1362–1378. https://doi.org/10.1002/esp.1478

Rickenmann, D., & McArdell, B. W. (2008). Calibration measurements with piezoelectric bedload impact sensors in the Pitzbach mountain stream. *Geodinamica Acta*, *21*, 35–52. https://doi.org/10.3166/ga.21.35-52

Rickenmann, D., & Fritschi, B. (2017). Bedload transport measurements with impact plate geophones in two Austrian mountain streams (Fischbach and Ruetz): system calibration, grain size estimation, and environmental signal pick-up. *Earth Surface Dynamics*, *5*(4): 669-687. https://doi.org/10.5194/esurf-5-669-2017

Rickenmann, D., Turowski, J. M., Fritschi, B., Klaiber, A., & Ludwig, A. (2012). Bedload transport measurements at the Erlenbach stream withgeophones and automated basket samplers. *Earth Surface Processes and Landforms*, *37*(9), 1000–1011. https://doi.org/10.1002/esp.3225

Rickenmann, D., Turowski, J. M., Fritschi, B., Wyss, C., Laronne J.B., Barzilai, R., et al. (2014). Bedload transport measurements with impact plate geophones: comparison of sensor calibration in different gravel-bed streams. *Earth Surface Processes and Landforms*, *39*, 928–942. https://doi.org/10.1002/esp.3499

Roth, D. L., Brodsky, E. E., Finnegan, N. J., Rickenmann, D., Turowski, J.M., & Badoux, A. (2016). Bed load sediment transport inferred from seismic signals near a river. *Journal of Geophysical Research Earth Surface*, *121*, 725-747. https://doi.org/10.1002/2015JF003782

Speerli, J., Bachmann, A. K., Bieler, S., Schumacher, A., & Gysin, S. (2020). Auswirkungen des Klimawandels auf den Sedimenttransport. 48 pp. Federal Office for the Environment (FOEN), Bern, Switzerland.

Stoffel, M., Tiranti, D., & Huggel, C. (2014). Climate change impacts on mass movements - Case studies from the European Alps. *Science of The Total Environment*, *493*, 1255-1266. https://doi.org/10.1016/j.scitotenv.2014.02.102.

Thorne, P. D. (1986). Laboratory and marine measurements on the acoustic detection of sediment transport. *Journal of the Acoustic Society of America*, *80*, 899–910. https://doi.org/10.1121/1.393913

Wales, D. J., & Doye, J. P. K. (1997). Global Optimization by Basin-Hopping and the Lowest Energy Structures of Lennard-Jones Clusters Containing up to 110 Atoms. *Journal of Physical Chemistry A*, *101*(28), 5111–5116. https://doi.org/10.1021/jp970984n

Wyss, C. R., Rickenmann, D., Fritschi, B., Turowski, J., Weitbrecht, V., & Boes, R. (2016a). Measuring bed load transport rates by grain-size fraction using the Swiss plate geophone signal at the Erlenbach, *Journal of Hydraulic Engineering*, *142*(5). https://doi.org/10.1061/(ASCE)HY.1943-7900.0001090,04016003

Wyss, C. R., Rickenmann, D., Fritschi, B., Turowski, J., Weitbrecht, V., & Boes, R. (2016b). Laboratory flume experiments with the Swiss plate geophone bed load monitoring system: 1. Impulse counts and particle size identification. *Water Resources Research*, 52, 7744–7759. https://doi.org/10.1002/2015WR018555

Wyss, C. R., Rickenmann, D., Fritschi, B., Turowski, J., Weitbrecht, V., Travaglini E, et al. (2016c). Laboratory flume experiments with the Swiss plate geophone bed load monitoring system: 2. Application to field sites with direct bed load samples. *Water Resources Research*, *52*, 7760–7778. https://doi.org/10.1002/2016WR019283